Applied Catalysis B: Environmental 206 (2017) 547–555

Contents lists available at ScienceDirect

Applied Catalysis B: Environmental

journal homepage: www.elsevier.com/locate/apcatb

Nano-structured rhodium doped $SrTiO_3$–Visible light activated photocatalyst for water decontamination

Borbala Kiss[a], Troy D. Manning[a], David Hesp[b], Christophe Didier[a], Arthur Taylor[c], David M. Pickup[d], Alan V. Chadwick[d], Heather E. Allison[e], Vinod R. Dhanak[b], John B. Claridge[a], James R. Darwent[a], Matthew J. Rosseinsky[a,*]

[a] Department of Chemistry, University of Liverpool, Crown Street, Liverpool L69 7ZD, UK
[b] Department of Physics and Stephenson Institute for Renewable Energy, University of Liverpool,Oxford Street, Liverpool L69 7ZE, UK
[c] Department of Cellular and Molecular Physiology, Institute of Translational Medicine, University of Liverpool, Crown Street, Liverpool L69 3BX, UK
[d] School of Physical Sciences, University of Kent, Canterbury CT2 7NH, UK
[e] Institute of Integrative Biology, University of Liverpool, Crown Street, Liverpool L69 7ZB, UK

ARTICLE INFO

Article history:
Received 14 July 2016
Received in revised form
22 December 2016
Accepted 23 January 2017
Available online 24 January 2017

Keywords:
Photocatalysis
Anti-microbial
Water decontamination
Doped titanates

ABSTRACT

A modified hydrothermal synthesis, avoiding high temperature calcination, is used to produce nano-particulate rhodium doped strontium titanate in a single-step, maintaining the rhodium in the photocatalytically active +3 oxidation state as shown by X-ray spectroscopy. The photoactivity of the material is demonstrated through the decomposition of aqueous methyl orange and the killing of *Escherichia coli* in aqueous suspension, both under visible light activation. A sample of $SrTiO_3$ containing 5 at% Rh completely decomposed a solution of methyl orange in less than 40 min and *E. coli* is deactivated within 6 h under visible light irradiation.

1. Introduction

Photocatalysis by semiconductor particles has been an active area of research since the 1970's [1]. The main drive for this work has been solar energy conversion via water splitting. More recently attention has focused on the use of photocatalysts for water treatment, specifically the photo-oxidation of dyes and organic contaminants [2]. There are also an increasing numbers of reports about the application of photocatalysts, especially TiO_2, for the treatment of bacteria and antimicrobial benefits [3,4].

TiO_2 is the most widely studied photocatalyst due to its high efficiency and stability when used as a photocatalyst in water however it has a large band gap and is restricted to UV photocatalysis [1,5]. In applications using sunlight, this limits it to utilising less than 5% of the solar spectrum and there is significant interest in extending the response of the material to visible light by doping with transition metals [5,6]. In solar energy conversion Kudo and others have shown that Rh-doped $SrTiO_3$ can be an efficient photocatalyst with visible light [7]. The role of Rh in this material is complicated by the availability of multiple oxidation states on Rh, particularly Rh^{3+} and Rh^{4+}. $SrTiO_3$ containing Rh^{4+} tends to be less photochemically active than the material containing only Rh^{3+} [8]. In this work we have modified the hydrothermal protocol of Kato et al. to avoid the need for high temperature calcination [9]. This produces a high surface area material and limits the amount of unwanted Rh^{4+} produced during high temperature calcination. We show that this form of Rh-doped $SrTiO_3$, in an aqueous suspension, is an efficient photocatalyst for dye oxidation and the destruction of bacteria with visible light, both important functionalities in the remediation of contaminated water.

2. Experimental

Further experimental details are provided in the Electronic Supplementary Information.

2.1. Photocatalyst synthesis

Nanostructured $SrTiO_3$ particles can be synthesized hydrothermally at temperatures between 100 and 200 °C by reacting

* Corresponding author.
E-mail address: m.j.rosseinsky@liverpool.ac.uk (M.J. Rosseinsky).

http://dx.doi.org/10.1016/j.apcatb.2017.01.066

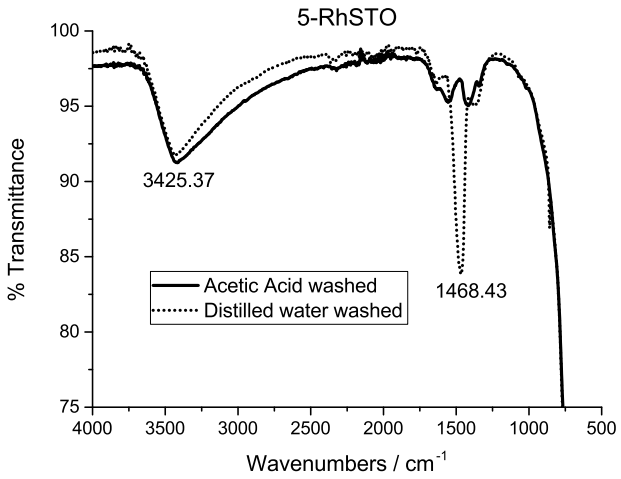

Fig. 1. FTIR spectra of acetic acid washed and distilled water washed 5-RhSTO showing the removal of residual $Sr(CO_3)_2$ (CO_3^{2-} stretch at 1468 cm^{-1}) by acetic acid washing.

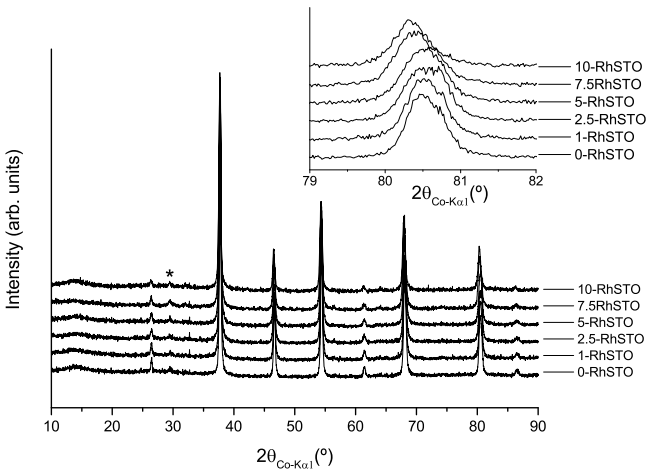

Fig. 2. PXRD pattern, using Co Kα radiation, of hydrothermally made Rh-doped $SrTiO_3$ samples with increasing Rh doping level (x = 0.0; 0.01; 0.025; 0.05; 0.075; 0.1). * anatase TiO_2. Inset–zoomed section between 79° and 82° showing increasing d-spacing with increased Rh doping.

nanoparticulate TiO_2 particles with an alkaline solution (pH > 12) of $Sr(OH)_2$. [9–11]. $SrTi_{1-x}Rh_xO_3$ (x = 0; 0.01; 0.025; 0.050; 0.075; 0.1) was prepared from Aeroxide® TiO_2 P25 (Sigma Aldrich, 99.5 %), $Sr(OH)_2 \cdot 8H_2O$ (Sigma Aldrich, 95 %), and $RhCl_3 \cdot xH_2O$ (Sigma Aldrich, Rh 38–40 %), mixed in 60 mL of distilled water at room temperature, using 2% excess of $Sr(OH)_2 \cdot 8H_2O$. The hydrothermal reaction was carried out in a 125 mL Teflon-coated reactor, placed in an oven at 180 °C for 12 h, 5 °C/min heating rate, 2 °C/min cooling rate. The synthesized oxides were washed by centrifuging twice with 1 M acetic acid and then twice with distilled water. The centrifuged product was dried at 60 °C in air. The yield of the product was 1.2 g, 44 % when 7.5 mmol of starting materials were used. After the synthetic reaction washing the slurry with organic acid (formic acid, acetic acid) removes the residual $SrCO_3$ (Fig. 1) [10]. A further calcination step was not performed on the material.

2.2. Photocatalytic dye degradation

The photocatalytic oxidation of methyl orange (MO) was performed according to a previously reported procedure [12] using visible light irradiation (λ > 420 nm). The reaction suspensions were prepared by adding the catalyst (0.1 g) to 100 mL of 0.02 g/L MO solution. The as-made suspension was purged with air during the whole reaction. The suspension was stirred in the dark overnight to ensure adsorption/desorption equilibrium of the dye has been attained on the surface of the catalyst prior to irradiation. During irradiation, 4 mL of the suspension was removed at 15 min intervals for subsequent MO concentration analysis following filtering through a 0.2 μm syringe filter. The absorption spectra of the aliquots were recorded in the range of 240–720 nm to determine the rate of MO degradation. The pH of the MO solution remained constant throughout the time reaction during the decomposition process (pH 7.2–7.7), no further adjustment was needed.

2.3. Photocatalytic killing of E. coli

Bacterial overnight cultures were set up by transferring a single bacterial colony from a streak plate to 10 mL Luria-Bertani (LB) broth for *E. coli* (strain MC1061) [13] and incubated at 37 °C overnight with shaking at 200 rpm. The overnight bacterial cultures were then sub-cultured and 250 μL was transferred to 10 mL fresh LB broth. The subculture was incubated at 37 °C until they reached mid-log growth phase ($O{\cdot}D_{\cdot 600}$ = ~0.4–0.5), when the sub-cultures (5 μL) were transferred to 5 mL of pre-autoclaved photocatalyst suspensions in aqueous phosphate buffered saline (PBS). For each time course experiment four samples were prepared: **L** (Light) – photocatalyst and *E. coli* sub-culture, exposed to visible light (λ > 420 nm); **D** (Dark) – photocatalyst and *E. coli*, covered to prevent exposed to light; **CL** (Control Light) – *E. coli* only, no photocatalyst, exposed to visible light (λ > 420 nm); **CD** (Control Dark) – *E. coli* only, no photocatalyst, covered to prevent exposure to light. During the reaction, the cells in the photocatalyst suspensions were stirred with magnetic stirrer bars. 100 μL samples were taken at 0 min, 120 min, 240 min and 360 min and diluted in 900 μL aq. PBS in a dilution series from 10^0 to 10^{-5}. In order to make up the cell dilutions in PBS and also to make the dilution series representative for plating, the harvested samples were vortexed and 20 μL of each dilution was spot plated in duplicate on LB agar plates and incubated overnight at 37 °C [14]. The bacterial colonies were then counted and colony forming units (CFU) mL^{-1} were calculated.

3. Results and discussion

3.1. Material characterisation

A series of Rh-doped $SrTiO_3$ samples were prepared by a hydrothermal method without a further calcination step, with Rh substituting for Ti ($SrTi_{1-x}Rh_xO_3$). Nominal Rh contents where x = 0, 0.01 (1 at%), 0.025 (2.5 at%), 0.05 (5 at%), 0.075 (7.5 at%) and 0.10 (10 at%) were prepared. Herein samples are referred to as X-RhSTO, where X is the at% of Rh.

Powder X-ray diffraction (PXRD) data of hydrothermally synthesised $SrTi_{1-x}Rh_xO_3$ samples (Fig. 2) can be indexed to a cubic unit cell with the $Pm\bar{3}m$ space group. The Scherrer equation gave primary $SrTi_{1-x}Rh_xO_3$ crystallite sizes of 29–35 nm, confirmed by transmission electron microscopy (TEM), (Fig. 3). Anatase TiO_2 (29.3 2θ, Co Kα) was present as an impurity phase in all samples (Fig. 2).

A plot of lattice parameter against measured Rh content is shown in Fig. 4. A linear evolution of lattice parameter was not observed in these samples and the lattice parameters are significantly larger than samples prepared by a solid-state route (Figure S1); a = 3.91624(9) Å for 0-RhSTO compared to 3.9056(1) Å for the equivalent solid-state sample. To explore the discrepancy between the lattice parameters of solid state and hydrothermally synthesised materials thermogravimetric analysis of the hydrothermally synthesised materials was performed (Fig. 5) which showed a

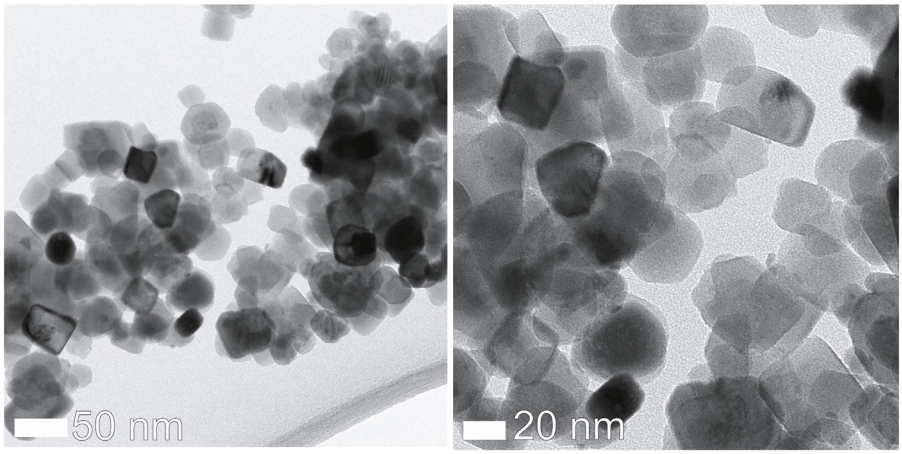

Fig. 3. TEM images of 5-RhSTO showing nanoparticles with sizes 20–50 nm.

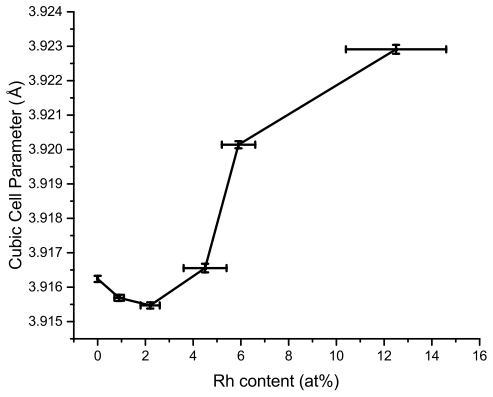

Fig. 4. Plot of lattice parameter against measured Rh at% in hydrothermally synthesised Rh doped $SrTiO_3$.

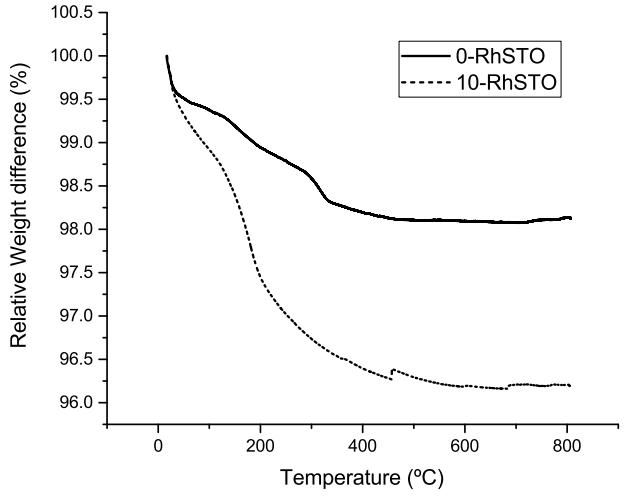

Fig. 5. TGA plot of 0-RhSTO and 10-RhSTO, between room temperature and 800 °C.

decrease in mass up to 450 °C corresponding to loss of hydroxyl groups, detected by FTIR as a broad peak around 3400 cm^{-1} (Fig. 1) [15]. The hydroxyl groups are present through hydration of the material, as also identified in $BaTiO_3$ [16], in the hydrothermal method and are also required for charge compensation of Rh^{3+}. This suggests there is an interplay between hydrating and charge compensating hydroxyl groups and Rh^{3+} all causing the lattice to expand by different amounts, and hence deviating from the ideal of Vegard's law.

Low magnification scanning electron microscopy (SEM) images of the materials show large (10–100 μm), non-uniform particles with some apparent porosity (Fig. 6a and b). At higher magnification these large particles were resolved into clusters of small particles with a size range of 50–100 nm (Fig. 6c and d), concurring with the primary particle size calculated from the PXRD and TEM. The individual particles appear to be fused/sintered to form a porous structure in the larger clusters (Fig. 6d). The morphology is consistent throughout the range of doping investigated (Fig. 6 and Figure S2). Nitrogen absorption-desorption isotherms of representative samples were measured (Figure S3) to give a surface area of 23 m^2/g, with a pore volume of 0.13 cm^3/g for 0-RhSTO, and 27 m^2/g, with a pore volume of 0.18 cm^3/g, for 1-RhSTO. These characteristics are reduced from the P25 starting material which has a surface area of 54 m^2/g and pore volume of 0.15 cm^3/g.

X-ray absorption near-edge spectroscopy (XANES) and X-ray photoelectron spectroscopy (XPS) were used to determine the oxidation state of Rh in the bulk and on the surface of samples 1-RhSTO, 5-RhSTO and 10-RhSTO. The Rh X-ray absorption edges of the samples were compared to those of $LaRhO_3$ (Rh^{3+}) and Sr_4RhO_6 (Rh^{4+}), where the Rh ions are in similar coordination environments to the doped $SrTiO_3$ materials. XPS spectra were compared to Rh foil (Figure S4), Rh_2O_3 (Figure S5) and literature values. It was not possible to obtain a satisfactory XANES of 1-RhSTO due to the low amount of Rh, however the Rh $3d_{5/2}$ XPS showed a symmetrical peak shape with a binding energy of 308.5 eV (*c.f.* Rh $3d_{5/2}$ in Rh_2O_3 at 308.4 eV, Figure S5, Table S2) indicating only Rh^{3+} at the surface (Fig. 7a) of this sample.

XANES spectra, collected in fluorescence geometry, for samples 5-RhSTO and 10-RhSTO are shown in Fig. 8. The absorption edge, E_0, was calculated as the zero point of the 2nd derivative. Energy shifts due to misalignment of the monochromotor were corrected by adjusting the relative absorption edge energy of the reference Rh^0, measured simultaneously to the samples, to that of the known absorption edge of Rh^0 (23.2199 keV) [17]. Corrected E_0 values for samples and standards are given in Table 1. The results suggest that Rh in these hydrothermally synthesised $SrTi_{1-x}Rh_xO_3$ is mostly in the +3 oxidiation state.

The Rh $3d_{5/2}$ XPS for the samples 5-RhSTO and 10-RhSTO show an asymmetric peak shape which could be deconvoluted into two peaks at 308.4 eV and 309.8 eV assigned to Rh^{3+} and Rh^{4+} species respectively (Fig. 7a), confirming the presence of the photoactive Rh^{3+} species in the material and the presence of Rh^{4+} on the surface. Fitting parameters for XPS are given in Supplementary Information

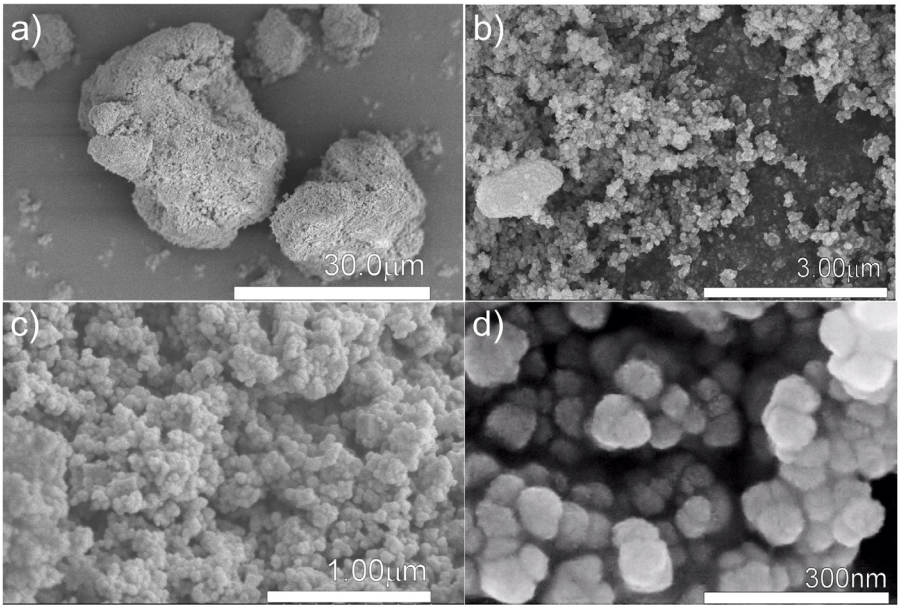

Fig. 6. SEM images of 0-RhSTO **(a, d)** and 5-RhSTO **(b, c)** samples, illustrating the agglomeration of the primary nanoparticulate materials.

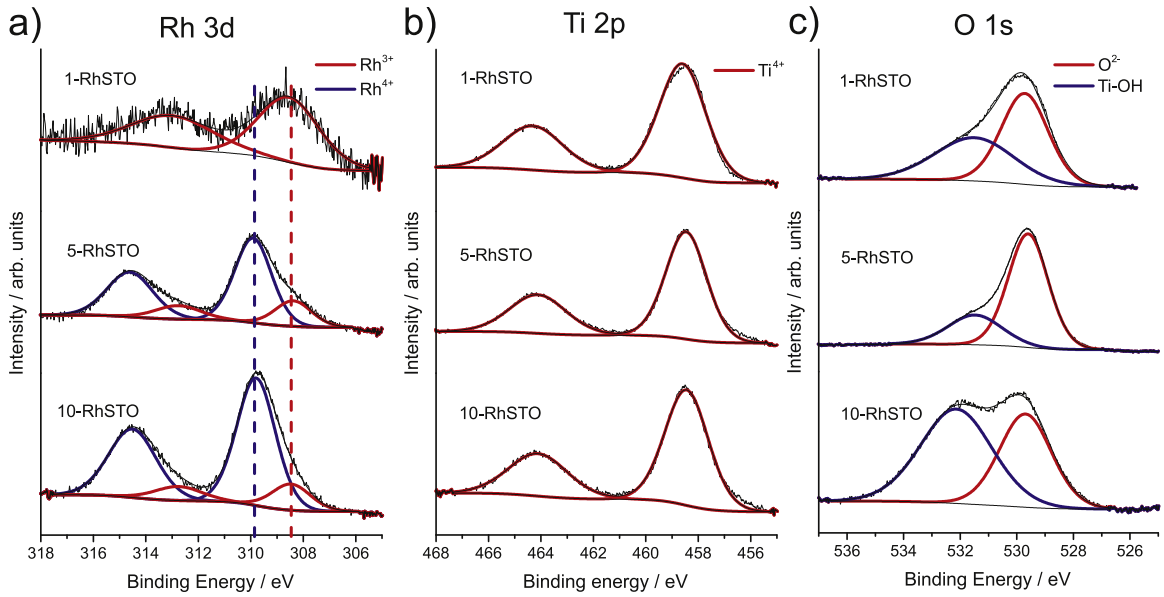

Fig. 7. (a) Fitted Rh 3d XPS spectrum of 1-RhSTO; 5-RhSTO and 10-RhSTO samples (Black line–original data, red line–Rh^{3+} fit and blue line–Rh4+ fit). (b) Fitted Ti 2p XPS spectrum of 1-RhSTO; 5-RhSTO and 10-RhSTO samples (Black line – original data, red curve – Ti^{4+} fit). (c) Fitted O 1 s XPS spectrum of 1-RhSTO; 5-RhSTO and 10-RhSTO samples (Black line–experimental data, red curve–superposition of O2- species, blue curve– –OH component. (For interpretation of the references to colour in this figure legend, the reader is referred to the web version of this article.)

Table 1
Rh X-ray absorption edges for standard materials and samples with x = 0.05, 0.10. Estimated errors.

Sample	E_0 (keV)
$LaRhO_3$ (Rh^{3+} standard)	23.2218(1)
Sr_4RhO_6 (Rh^{4+} standard)	23.2227(1)
5-RhSTO	23.2218(2)
10-RhSTO	23.2217(2)

(Tables S3-S5). The doping limit of Rh into $SrTiO_3$ determined from solid-state synthesis was at ~6 at%, hence the presence of RhO_2 is unsurprising at high Rh amounts. All Rh measured binding energies match well with literature values [18–23] and standard materials (Tables S1 and S2). In the Ti 2p XPS spectral region (Fig. 7b), there are 2 symmetrical peaks at 464.2 eV and 458.5 eV binding energies that can be attributed to Ti $2p_{1/2}$ and Ti $2p_{3/2}$ levels of Ti^{4+} in oxide [24]. No other Ti species were detected.

In the O 1 s spectra the asymmetric peak is assigned to the O^{2-} species at 529.7 eV binding energy characteristic of oxide materials [25]. The shoulder observed at 531.5 eV can be attributed to the Ti-OH species [25] (Fig. 7c). No O1 s peak arising from carboxyl oxygen in acetic acid is observed at ~533 eV [25], indicating that the acetic acid used to remove unreacted $SrCO_3$, is completely removed after distilled water washing, agreeing with the FTIR measurement (Fig. 1). XPS did not show any Cl $2p_{3/2}$ at 199.1 eV binding energy even for sample 10-RhSTO, indicating that unreacted $RhCl_3$ or chloride contamination was not present in the samples.

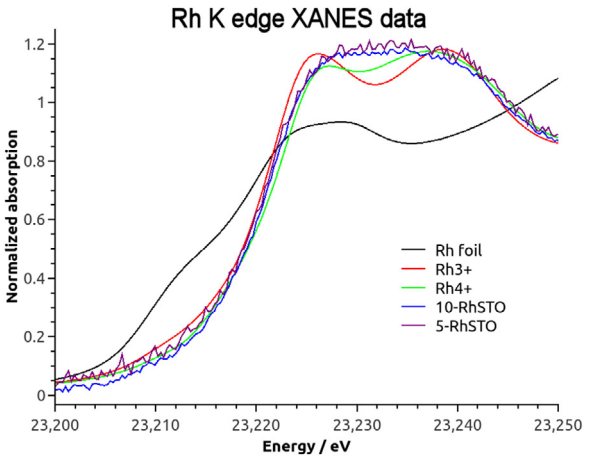

Fig. 8. Corrected XANES spectra of 5-RhSTO, 10-RhSTO and standard samples.

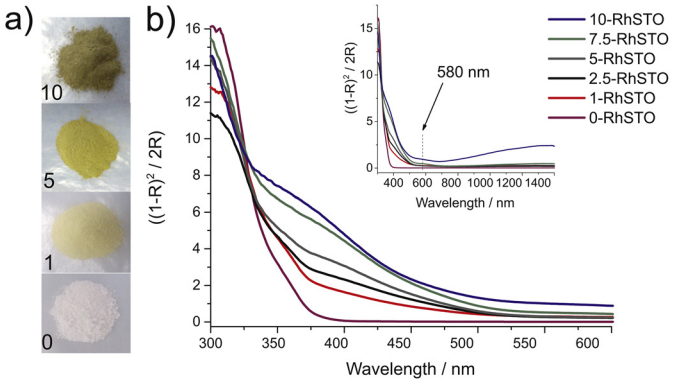

Fig. 9. **(a)** Colour change of X-RhSTO samples upon Rh doping level X = 0; 1; 5; 10 and **(b)** Kubelka-Munk function of as-made samples for X = 0; 1; 2.5; 5; 7.5; 10, (inset full spectra 300–1400 nm showing broad absorption in the NIR).

Table 2
Calculated band gaps from fitting the Kubelka-Munk absorption spectra of X-RhSTO to a combined power law, exponential and Gaussian function (Standard error given in brackets).

Rh at% (X-RhSTO)	Fitted Band gap (eV)
0	3.19(1)
1	3.17(1)
2.5	3.19(3)
5	3.18(4)
7.5	3.09(5)
10	2.92(9)

The XANES and XPS results show that the hydrothermal method, without a high temperature calcination step, produces nanosized Rh doped $SrTiO_3$ with the dopant mostly in the +3 oxidation state, with a general formula $SrTi_{1-x}Rh_x(III)O_{3-x/2}(OH)_x$.

The determination of optical band gaps directly from Tauc type plots for materials containing d–d transitions can be difficult due to overlap of the various contributions to the optical spectrum (Fig. 9). Fitting of the Kubelka-Munk spectra, between 1.85 eV and 4 eV, to a power law function for an indirect band gap and an exponential function for the Urbach tail, plus a Gaussian function for the Rh d–d transitions [26] gave optical band gaps shown in Table 2 (see Figure S6 and S7 and Table S5 for fitting). The fundamental valence band to conduction band transition of the material is not changed significantly for $x \leq 0.05$ and only decreases with higher Rh loadings, $x > 0.05$. The reported band structure calculated by density functional theory (DFT) [8,27] shows a Rh t_{2g}-state immediately above the valence band and the transition from this state

Table 3
Strontium ICP-OES results from 5-RhSTO suspended in PBS at four different concentrations.[b]

Photocatalyst Concentration (% w/V)[a]	Dissolved Sr concentration (ppm)[c]
0.05	2.5
0.1	5.0
0.5	17.6
1	24.7

[a] Freshly prepared catalyst suspension, no bacteria cells were added.
[b] No Rh or Ti was detected in any of the samples. ICP-OES detection limit for Rh = 0.1 ppm; Ti = 5×10^{-3} ppm.
[c] ICP-OES detection limit for Sr = 5×10^{-4} ppm.

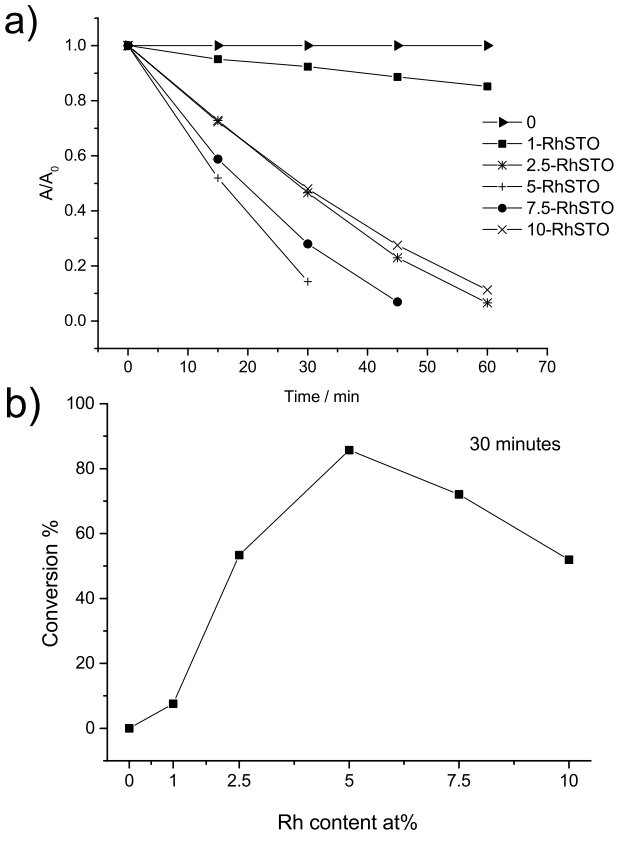

Fig. 10. **(a)** MO degradation under visible light reaction of $SrTi_{1-x}Rh_xO_3$ (x = 0; 0.01; 0.025; 0.05; 0.075; 0.1) samples over a 1 h time scale; **(b)** Trend of MO conversion after 30 min using the as-made catalysts.

to the conduction band can be assigned to the optical absorption at around 380 nm and giving rise to the yellow colour observed in the samples with $0.01 \leq x < 0.075$ (Fig. 9a). At higher concentrations of Rh ($x \geq 0.075$ there was a second absorption band around 580 nm and a broad peak stretching into the near infrared with a maximum at 1300 nm both attributable to the surface Rh^{4+} d–d transitions [7]. The diffuse reflectance measurement of the $x \leq 0.05$ sample shows limited absorption at this region, indicating predominantly Rh^{3+} in the structure, in good agreement with the XANES and XPS results.

3.2. Photocatalytic dye degradation

The visible light activated photocatalytic efficiency of as-made samples were tested for azo-dye degradation. Fig. 10 shows the photocatalytic activity for methyl orange (MO) degradation reaction using visible light ($\lambda > 420$ nm). MO has been widely used as a probe for the photocatalytic oxidation of dyes using UV light absorbing materials such as TiO_2. The results show that X-RhSTO

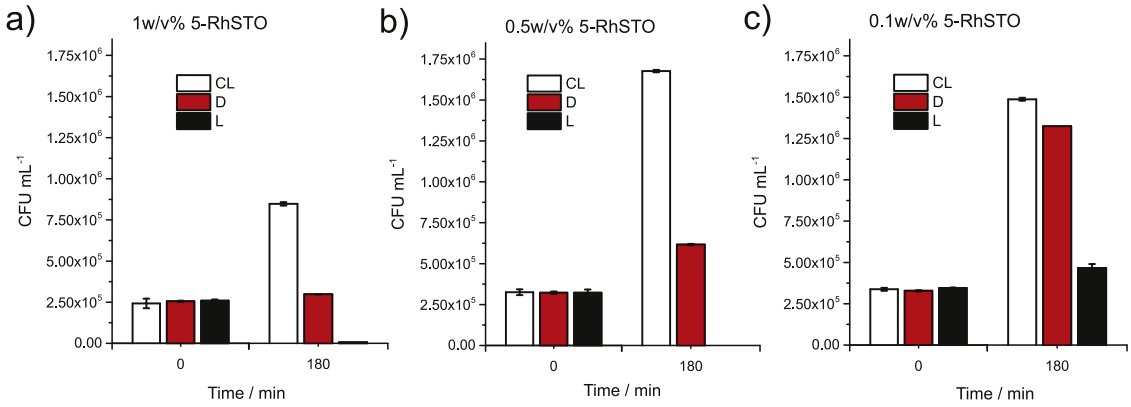

Fig. 11. Representative plots of viable *E. coli* population (colony forming units mL^{-1}) after 0 min and 180 min with catalyst concentrations of **(a)** 1% w/V of 5-RhSTO, **(b)** 0.5% w/V of 5-RhSTO and **(c)** 0.1% w/V of 5-RhSTO under control light (CL–white bars), dark (D–red bars) and light (L–black bars) conditions; 300 W Xenon lamp (λ > 420 nm); error bars denote the standard deviations of CFU mL^{-1} units for each experiment.

Table 4
ICP-OES results of 0.1% w/V 5-RhSTO and 0.1% w/V 0-RhSTO suspended in PBS at various photocatalytic reaction conditions, the blank PBS solution and the LB broth in PBS.[d,e]

Nominal Rh at%	Conditions	Sr/(ppm)[e]
5	Autoclaved catalyst in PBS buffer + 24 h stirring in "Dark" + 2nd autoclaving, centrifuging, filtering off the particles[a,f]	5.023
5	Autoclaved catalyst. in PBS buffer + 24 h stirring in "Light" + 2nd autoclaving, centrifuging, filtering off the particles[a,f]	5.301
5	Autoclaved catalyst in PBS buffer + 24 h stirring in "Dark" + Cells + 2nd autoclaving, centrifuging, filtering off the particles[b,f]	6.545
5	Autoclaved catalyst in PBS buffer + 24 h stirring in "Light" + Cells + 2nd autoclaving, centrifuging, filtering off the particles[b,f]	4.749
N/A	Phosphate Buffered Saline (PBS)	0.010
N/A	LB broth + PBS (5 μL LB broth in 5 mL PBS)	0.024
0	Autoclaved catalyst in PBS buffer + 24 h stirring in "Dark" + Cells + 2nd autoclaving, centrifuging, filtering off the particles[c,f]	6.655
0	Autoclaved catalyst in PBS buffer + 24 h stirring in "Light" + Cells + 2nd autoclaving, centrifuging, filtering off the particles[c,f]	7.220
0	Catalyst in PBS buffer + 24 h stirring in "Dark" + no autoclaving, centrifuging, filtering off the particles[a]	6.030
0	Catalyst in distilled water + 24 h stirring in "Dark" + no autoclaving, centrifuging, filtering off the particles[a]	5.677

[a] Freshly prepared catalyst suspension with no bacteria cells were added.
[b] One repeat of **L** experiment of Fig. 12.
[c] One repeat of **L** experiment of Fig. 13.
[d] No Rh was detected in any of the samples. ICP-OES detection limit for Rh = 0.1 ppm.
[e] ICP-OES detection limit for Sr = 5×10^{-4} ppm.
[f] Autoclave: high pressure saturated steam at 121 °C, 15–20 min.

is remarkably active as a visible light photocatalyst leading to the almost complete destruction of the dye in less than 1 h.

The azo-dye degradation by X-RhSTO samples follows first order reaction kinetics. 5-RhSTO sample showed the best performance in photocatalytic activity. Within 30 min 86 % of MO was destroyed with a reaction rate, $k = 0.065\ min^{-1}$ (Fig. 10a). This is comparable to the activity of P25 TiO_2 under UV illumination ($k = 0.10\ min^{-1}$) [12]; P25 TiO_2 is not active under visible light irradiation [2,28]. The high visible light activity of X-RhSTO can be attributed to the high surface area and the Rh^{3+} oxidation state of species up to X = 5. Increasing the doping level X > 5 introduces Rh^{4+} which can act as a recombination site for the photogenerated charge carriers and therefore suppress the kinetic reaction rate [7]. The parent compound showed no activity in MO degradation in a control experiment upon visible light exposure (Fig. 10, Figure S8).

The activity of the X-RhSTO materials compares favourably to materials such as Cr-doped $SrTiO_3$—C_3N_4 composites ($k = 0.012\ min^{-1}$) [29] Pt-$CaCu_3Ti_4O_{12}$ ($k = 0.0045\ min^{-1}$) [12], that used similar conditions to those in this work; or Mo- and S-codoped TiO_2 ($k = 0.019\ min^{-1}$) [30] that was tested under more intense light irradiation.

3.3. Photocatalytic treatment of bacteria

5-RhSTO, showing the highest activity for MO degradation, was tested for the photocatalytic killing of the Gram negative bacteria *E. coli* in aqueous suspension. The suspension concentration was optimised to avoid any toxicity effect due to the photocatalyst. Fig. 11 shows the viable *E. coli* population as colony forming units per mL (CFU mL^{-1}) in a PBS suspension with 5-RhSTO after sampling and plating them on Luria broth (LB) agar under control light (**CL** – visible light exposure, no photocatalyst), dark (**D** – no light exposure, with photocatalyst) and light (**L** – visible light exposure, with photocatalyst) conditions. At the catalyst suspension concen-

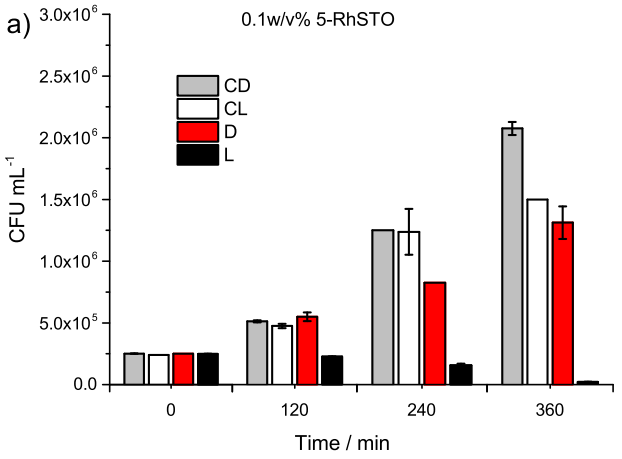

Fig. 12. Representative plot of CFU mL^{-1} time line measurement of E. coli population with concentration of 0.1% w/V of doped 5-RhSTO under control dark, control light, dark and light conditions; 300 W Xenon lamp (λ > 420 nm); error bars denote the standard deviations of CFU mL^{-1} units for the individual experiment.

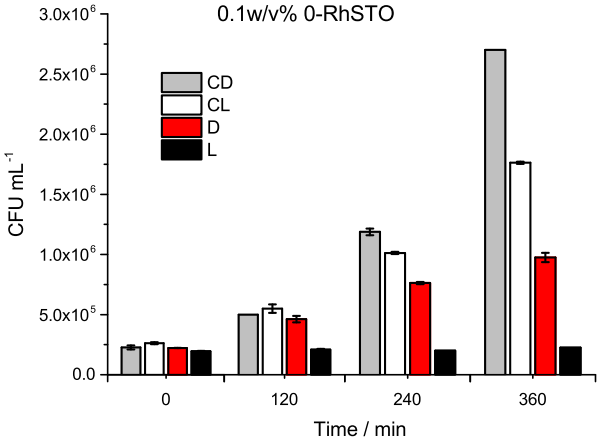

Fig. 13. Representative plot of CFU mL^{-1} of *E. coli* over time were determined using a concentration of 0.1% w/V of undoped $SrTiO_3$ under control dark (CD), control light (CL), dark (D) and light (L), conditions using a 300 W Xenon lamp (λ > 420 nm); error bars denote the standard deviations of CFU mL^{-1} units the individual experiment.

trations of 1.0 and 0.5 w/V%, toxicity appeared after 180 min as the *E. coli* growth was inhibited even under **D** condition compared to the **CL** experiment when the catalyst was not present (Fig. 11a and b). At a photocatalyst suspension concentration of 0.1 w/V% the **D** experiment shows similar numbers of CFUs to the **CL** 180 min indicating the photocatalyst is below the toxic limit for *E. coli*, and any reduction in *E. coli* CFUs is due to the photocatalytic activity of the material (Fig. 11c). Inductively coupled plasma optical emission spectroscopy (ICP-OES) analysis of the supernatants was carried out in order to investigate the catalyst stability under the photocatalytic conditions. For this, the 5-RhSTO catalyst was suspended in PBS buffer, stirred for 24 h in the dark, centrifuged at 10,000 rpm for 10 min and the particles were filtered off with a d > 0.2 μm pore size syringe filter. The various suspension concentrations are shown in Table 3.

The measured data indicate Rh or Ti were present below the detection limits of the ICP-OES measurement in all of the supernatants, however, dissolved strontium was shown to increase with increasing amounts of catalyst in suspension from 0.05–1% w/V respectively. *E. coli* appears to be resistant to strontium concentrations of up to 5 ppm. This concentration of strontium was consistent throughout all of the photocatalytic conditions used subsequently (Table 4) and comparable to the solubility of $SrCO_3$ at room temperature (11 ppm). The hydrothermally synthesised materials in this study show improved stability compared to solid-state synthesised $SrTi_{1-x}Fe_xO_3$ at suspension concentration of 0.1% w/V, where 49 ppm of Sr was detected in the supernatant and showed significant toxic effects to *E. coli* [4]. Our studies show that ~17 ppm of Sr can result in toxic effects towards *E. coli* (Fig. 11b). Moreover, it should also be noted that the ICP-OES detection limit for Rh is 0.1 ppm and the effective harmful concentration of Rh is reported to be three orders of magnitude greater [31].

To examine the impact of the catalyst on *E. coli* cell numbers over time, culture samples were taken every 120 min over a six hour period using 0.1 w/V% 5-RhSTO catalyst, under control dark (**CD** – no light exposure, no photocatalyst), control light (**CL** – light exposure, no photocatalyst), dark (**D** – no light, with photocatalyst) and light (**L** – light exposure, with photocatalyst) conditions. The experiments were repeated three times with representative data shown in Fig. 12 and Table 5 (all repeats showed similar trends, Figure S10).

After 120 min the number of CFUs of *E. coli* in the **L** experiment exhibits a clear difference to the other conditions, showing no change in the number of CFUs from the initial number, compared to the **CL**, **CD** and **D** where significantly more CFUs are observed. After 360 min the number of CFUs in the **L** experiment significantly decreases to 9% of the original cell numbers. As a comparison when no catalyst was added to the PBS suspension in the **CD** experiment the number of CFUs increases by an order of magnitude.

Table 5
E. coli CFUs at T_0 and at T_{360} min with catalyst concentration of 0.1 w/V% 5-RhSTO under control dark, control light, dark and light conditions; 300 W Xenon lamp (λ > 420 nm).

Conditions	$T_0 \times 10^5$ CFU mL^{-1}	$T_{360} \times 10^5$ CFU mL^{-1}
CD	2.51	20.8
CL	2.40	15.0
D	2.50	13.1
L	2.49	0.225

Table 6
E. coli CFUs at T_0 and at T_{360} min with catalyst concentration of 0.1 w/V% 0-RhSTO under control dark, control light, dark and light conditions; 300 W Xenon lamp (λ > 420 nm).

Conditions	$T_{0\times} 10^5$ CFU mL^{-1}	$T_{360\times} 10^5$ CFU mL^{-1}
CD	2.26	27.0
CL	2.63	17.6
D	2.23	9.75
L	1.95	2.25

As a control experiment, undoped $SrTiO_3$ was also tested three times under the same conditions (Fig. 13 and Table 6, Figure S10). There was no apparent change in CFUs across the **L** experiment, suggesting an inhibition of cell growth/division rather than killing the cells upon exposure to light in the presence of $SrTiO_3$. This combination of inhibition and photocatalytic killing makes the 5-RhSTO material particularly effective in destroying *E. coli*.

In order to understand better the processes, fluorescent microscopy was used to visualise bacteria after plating and show possible cell death. The LIVE/DEAD BacLight Bacterial Viability Kit utilises mixtures of the SYTO® 9 green-fluorescent nucleic acid stain and the red-fluorescent nucleic acid stain, propidium iodide. These stains differ both in their spectral characteristics and in their ability to penetrate into healthy bacterial cells. When both dyes are premixed and added together to the cell culture, propidium iodide penetrates only into bacteria with damaged membranes, causing a reduction in the SYTO® 9 stain fluorescence and stains the cells red. The killing of the cells by visible light activated 5-RhSTO was visualised by fluorescent microscopy, taken in the 6th hour of each

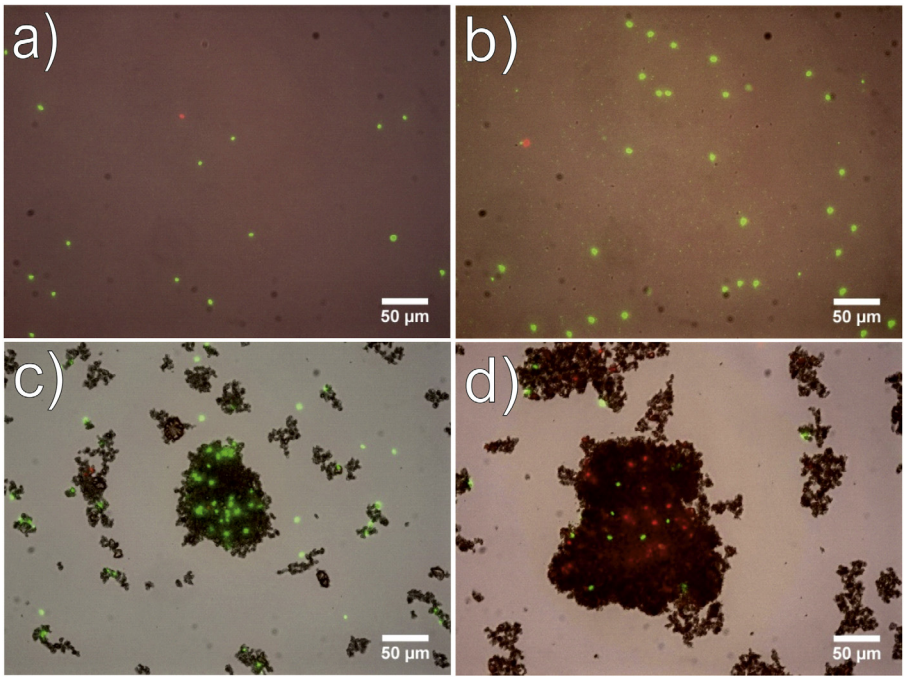

Fig. 14. *E. coli* cell population viability in the 6th hour of photocatalytic test detected by SYTO® 9 (green fluorescent) and Propidium Iodide (red fluorescent) nucleic acid stains. **(a)** Untreated cells in control dark and **(b)** control light experiments are viable. **(c)** Treated cells in dark experiment are viable. **(d)** Treated cells in light experiment are mostly destroyed; Catalyst 0.1% w/V 5-RhSTO; Light source 300W Xenon lamp (λ > 420 nm). (For interpretation of the references to colour in this figure legend, the reader is referred to the web version of this article.)

experiment (**CD, CL, D, L**). In the control experiments (Fig. 14a and b) the majority of cells are undamaged (fluorescing green). In the experiments containing photocatalyst (Fig. 14c and d) only those exposed to light shows significant damaged cells (fluorescing red).

It was observed that after removal from suspension, cells appear to be attached and agglomerated onto the catalyst. If this occurs during the photocatalytic experiments it may have an effect on the number of countable CFUs by underestimating the viable cells in the plating measurements, especially in the **D** experiment where is seems many live cells are agglomerated to the photocatalyst. It is also apparent that direct contact with the photocatayst is not toxic to *E. coli* as live cells are seen agglomerated to the photocatalyst not exposed to light. Only the photocatalyst exposed to light showed significant numbers of dead cells, confirming it is mostly a photocatalytic killing of the bacteria. If there is an affinity for the bacteria to the solid photocatalyst this may add an additional mechanism for removing harmful organisms by a simple filtration of photo-active particles. Therefore the photocatalyst could be classed as a "bioactive-filter" similar to the well-known silver-deposited activated carbon fibres (ACF) [32] proposed for use in industrial processes such as drinking water filtration.

4. Conclusions

Contamination of water by organic molecules and bacteria is a growing ecological and societal issue, leading to a need for simple and effective methods of decontamination. Here we demonstrate a one-step hydrothermal synthesis of $SrTi_{1-x}Rh_xO_3$, ($0 < x < 0.1$) giving a high surface area material displaying efficient visible light activated photocatalytic activity towards organic dye degradation and anti-microbial properties in aqueous suspension. When $x \leq 0.05$ the Rh dopant is predominantly in the Rh(III) oxidation state in the bulk of the material resulting in a very efficient visible-light (λ >420 nm) activated photocatalyst.

5-RhSTO is shown to completely oxidise a 0.02 g/L solution of methyl orange within 30 min under visible light illumination ($k = 0.065\ min^{-1}$), which is comparable to the activity of P25 TiO_2 under UV illumination of similar intensity ($k = 0.10\ min^{-1}$), and more active than doped TiO_2 materials showing visible light activity.

It is also shown that 5-RhSTO can act as an anti-microbial material to inhibit the growth of *E. coli* in aqueous suspension, effectively killing the bacteria within 6 h of visible light exposure.

The material shows potential for the visible light activated photo-decontamination of water containing organic molecules and bacteria.

Acknowledgements

This work was funded by EPSRC (EP/H000925) and through European Commission (FP7-PEOPLE-2007-214040). XANES experiments were performed under SP14239 as part of the Energy Materials BAG at the Diamond Light Source, UK on beam line B18. Thanks are extended to Dr Marco Zanella for SEM images, Dr Alexandros Katsoulidis for surface area and pore volume measurements and Mr George Miller for ICP-OES measurements.

Appendix A. Supplementary data

Supplementary data associated with this article can be found, in the online version, at http://dx.doi.org/10.1016/j.apcatb.2017.01.066. Underlying raw data associated with this article can be found at http://dx.doi.org/10.17638/datacat.liverpool.ac.uk/155.

References

[1] K. Liu, M. Cao, A. Fujishima, L. Jiang, Bio-inspired titanium dioxide materials with special wettability and their applications, Chem. Rev. 114 (2014) 10044–10094.
[2] G. Yang, Z. Jiang, H. Shi, T. Xiao, Z. Yan, Preparation of highly visible-light active N-doped TiO2 photocatalyst, J. Mater. Chem. 20 (2010) 5301–5309.

[3] M.N. Chong, B. Jin, C.W.K. Chow, C. Saint, Recent developments in photocatalytic water treatment technology: a review, Water Res. 44 (2010) 2997–3027.
[4] L. Zhang, P.Y. Tan, C.L. Chow, C.K. Lim, O.K. Tan, M.S. Tse, C.C. Sze, Antibacterial activities of mechanochemically synthesized perovskite strontium titanate ferrite metal oxide, Colloids Surf. A Physicochem. Eng. Asp. 456 (2014) 169–175.
[5] A. Kudo, R. Niishiro, A. Iwase, H. Kato, Effects of doping of metal cations on morphology, activity, and visible light response of photocatalysts, Chem. Phys. 339 (2007) 104–110.
[6] R. Asahi, T. Morikawa, T. Ohwaki, K. Aoki, Y. Taga, Visible-Light photocatalysis in nitrogen-doped titanium oxides, Science 293 (2001) 269–271.
[7] R. Konta, T. Ishii, H. Kato, A. Kudo, Photocatalytic activities of noble metal ion doped SrTiO3 under visible light irradiation, J. Phys. Chem. B 108 (2004) 8992–8995.
[8] S. Kawasaki, K. Akagi, K. Nakatsuji, S. Yamamoto, I. Matsuda, Y. Harada, J. Yoshinobu, F. Komori, R. Takahashi, M. Lippmaa, C. Sakai, H. Niwa, M. Oshima, K. Iwashina, A. Kudo, Elucidation of Rh-induced in-gap states of Rh:SrTiO3 visible-light-driven photocatalyst by soft X-ray spectroscopy and first-principles calculations, J. Phys. Chem. C 116 (2012) 24445–24448.
[9] H. Kato, Y. Sasaki, N. Shirakura, A. Kudo, Synthesis of highly active rhodium-doped SrTiO3 powders in Z-scheme systems for visible-light-driven photocatalytic overall water splitting, J. Mater. Chem. A 1 (2013) 12327–12333.
[10] Y. Wang, H. Xu, X. Wang, X. Zhang, H. Jia, L. Zhang, J. Qiu, A general approach to porous crystalline TiO2, SrTiO3, and BaTiO3 spheres, J. Phys. Chem. B 110 (2006) 13835–13840.
[11] S.W. Bae, P.H. Borse, J.S. Lee, Dopant dependent band gap tailoring of hydrothermally prepared cubic SrTixM1-xO3(M=Ru,Rh,Ir,Pt,Pd) nanoparticles as visible light photocatalysts, Appl. Phys. Lett. 92 (2008) 104107.
[12] J.H. Clark, M.S. Dyer, R.G. Palgrave, C.P. Ireland, J.R. Darwent, J.B. Claridge, M.J. Rosseinsky, Visible light photooxidation of model pollutants using CaCu3Ti4O12: an experimental and theoretical study of optical properties, electronic structure, and selectivity, J. Am. Chem. Soc. 133 (2011) 1016–1032.
[13] M.J. Casadaban, S.N. Cohen, Analysis of gene control signals by DNA fusion and cloning in Escherichia coli, J. Mol. Biol. 138 (1980) 179–207.
[14] A.A. Miles, S.S. Misra, J.O. Irwin, The estimation of the bactericidal power of the blood, Epidemiol. Infect. 38 (1938) 732–749.
[15] J.M.G. Amores, V.S. Escribano, M. Daturi, G. Busca, Preparation, characterization and surface structure of coprecipitated high-area Sr TiO2 +(0 [less-than-or-eq]x[less-than-or-eq] 1) powders, J. Mater. Chem. 6 (1996) 879–886.
[16] K.D. Kreuer, Proton-conducting oxides, Annu. Rev. Mater. Res. 33 (2003) 333–359.
[17] S. Kraft, J. Stümpel, P. Becker, U. Kuetgens, High resolution x-ray absorption spectroscopy with absolute energy calibration for the determination of absorption edge energies, Rev. Sci. Instrum. 67 (1996) 681–687.
[18] Z. Weng-Sieh, R. Gronsky, A.T. Bell, Microstructural evolution of γ-alumina-supported Rh upon aging in air, J. Catal. 170 (1997) 62–74.
[19] T.L. Barr, An ESCA study of the termination of the passivation of elemental metals, J. Phys. Chem. 82 (1978) 1801–1810.
[20] J.S. Brinen, A. Melera, Electron spectroscopy for chemical analysis (ESCA) studies on catalysts. Rhodium on charcoal, J. Phys. Chem. 76 (1972) 2525–2526.
[21] K. Maeda, K. Teramura, D. Lu, T. Takata, N. Saito, Y. Inoue, K. Domen, Characterization of Rh-Cr mixed-oxide nanoparticles dispersed on (Ga 1-xZnx)(N1-xOx) as a cocatalyst for visible-light-driven overall water splitting, J. Phys. Chem. B 110 (2006) 13753–13758.
[22] M. Zimowska, J.B. Wagner, J. Dziedzic, J. Camra, B. Borzęcka-Prokop, M. Najbar, Some aspects of metal-support strong interactions in Rh/Al 2O3 catalyst under oxidising and reducing conditions, Chem. Phys. Lett. 417 (2006) 137–142.
[23] H.W. Kang, S.B. Park, Preparation of novel SrTiO3:Rh/Ta photocatalyst by spray pyrolysis and its activity for H2 evolution from aqueous methanol solution under visible light, Int. J. Hydrogen Energy 38 (2013) 823–831.
[24] X. Chen, L. Liu, P.Y. Yu, S.S. Mao, Increasing solar absorption for photocatalysis with black hydrogenated titanium dioxide nanocrystals, Science 331 (2011) 746–750.
[25] E. McCafferty, J.P. Wightman, Determination of the concentration of surface hydroxyl groups on metal oxide films by a quantitative XPS method, Surf. Interface Anal. 26 (1998) 549–564.
[26] B. Kiss, C. Didier, T. Johnson, T.D. Manning, M.S. Dyer, A.J. Cowan, J.B. Claridge, J.R. Darwent, M.J. Rosseinsky, Photocatalytic water oxidation by a pyrochlore oxide upon irradiation with visible light: rhodium substitution into yttrium titanate, Angew. Chem. 126 (2014) 14708–14712.
[27] B. Modak, S.K. Ghosh, Origin of enhanced visible light driven water splitting by (Rh, Sb)-SrTiO3, Phys. Chem. Chem. Phys. 17 (2015) 15274–15283.
[28] X.-T. Zhou, H.-B. Ji, X.-J. Huang, Photocatalytic degradation of methyl orange over metalloporphyrins supported on TiO2 degussa P25, Molecules 17 (2012) 1149.
[29] M. Yang, X.-Q. Jin, Improvement of visible light-induced photocatalytic performance by Cr-doped SrTiO3-carbon nitride intercalation compound (CNIC) composite, J. Cent. South Univ. 23 (2016) 310–316.
[30] V. Jabbari, M. Hamadanian, M. Shamshiri, D. Villagran, Band gap and Schottky barrier engineered photocatalyst with promising solar light activity for water remediation, RSC Adv. 6 (2016) 15678–15685.
[31] B. Rosenberg, E. Renshaw, L. Vancamp, J. Hartwick, J. Drobnik, Platinum-induced filamentous growth in Escherichia coli, J. Bacteriol. 93 (1967) 716–721.
[32] K.Y. Yoon, J.H. Byeon, C.W. Park, J. Hwang, Antimicrobial effect of silver particles on bacterial contamination of activated carbon fibers, Environ. Sci. Technol. 42 (2008) 1251–1255.